Stability of Néel-type skyrmion lattice against oblique magnetic fields in GaV$_4$S$_8$ and GaV$_4$Se$_8$

B. Gross,[1] S. Philipp [◉],[1] K. Geirhos [◉],[2] A. Mehlin,[1] S. Bordács,[3,4] V. Tsurkan [◉],[2,5] A. Leonov,[6]
I. Kézsmárki,[2] and M. Poggio [◉][1,7]

[1]*Department of Physics, University of Basel, 4056 Basel, Switzerland*
[2]*Experimental Physics V, Center for Electronic Correlations and Magnetism, University of Augsburg, 86159 Augsburg, Germany*
[3]*Department of Physics, Budapest University of Technology and Economics, 1111 Budapest, Hungary*
[4]*Hungarian Academy of Sciences, Premium Postdoctor Program, 1051 Budapest, Hungary*
[5]*Institute of Applied Physics, MD-2028 Chisinau, Republic of Moldova*
[6]*Department of Chemistry, Faculty of Science, Hiroshima University Kagamiyama, Higashi Hiroshima, Hiroshima 739-8526, Japan*
[7]*Swiss Nanoscience Institute, University of Basel, 4056 Basel, Switzerland*

Nanometer-scale magnetization configurations known as magnetic skyrmions have mostly been studied in cubic chiral helimagnets, in which they are Bloch-type and their axes align along the applied magnetic field. In contrast, the orientation of Néel-type skyrmions is locked to the polar axis of the host material's underlying crystal structure. In the lacunar spinels GaV$_4$S$_8$ and GaV$_4$Se$_8$, the Néel-type skyrmion lattice phase exists for externally applied magnetic fields parallel to this axis and withstands oblique magnetic fields up to some critical angle. Here, we map out the stability of the skyrmion lattice phase in both crystals as a function of field angle and magnitude using dynamic cantilever magnetometry. The measured phase diagrams reproduce the major features predicted by a recent theoretical model, including a reentrant cycloidal phase in GaV$_4$Se$_8$. Nonetheless, we observe a greater robustness of the skyrmion phase to oblique fields, suggesting possible refinements to the model. Besides identifying transitions between the cycloidal, skyrmion lattice, and ferromagnetic states in the bulk, we measure additional anomalies in GaV$_4$Se$_8$ and assign them to magnetic states confined to polar structural domain walls.

I. INTRODUCTION

The discovery of the nanometer-scale magnetization configurations known as magnetic skyrmions [1] has spurred renewed interest in noncentrosymmetric magnets. The lack of inversion symmetry in these crystals gives rise to an asymmetric exchange coupling, known as the Dzyaloshinskii-Moriya interaction (DMI). Crystal symmetry determines the form of the free energy term corresponding to the DMI, which—in competition with the spin stiffness—stabilizes modulated spin-textures such as spirals and skyrmions and determines their internal structure [2,3]. Both skyrmion lattices (SkLs) [4,5] and isolated skyrmions [6] have now been observed in either bulk or nanostructured noncentrosymmetric crystals. Their topologically protected spin-texture, which is stable even at room temperature [7], their nanometer-scale size, and their easy manipulation via electric currents and fields [8–12] make skyrmions a promising platform for information storage and processing applications [13,14].

Until recently, most investigations in bulk crystals focused on Bloch-type skyrmions, in which the local magnetization rotates perpendicular to the radial direction moving from the skyrmion core to the far field. This type of skyrmion was observed in chiral cubic helimagnets with B20 structure such as MnSi [1], FeGe [15], or Cu$_2$OSeO$_3$ [16]. Recently, Néel-type skyrmions, in which the local magnetization rotates in

a plane containing the radial direction, were observed in bulk GaV$_4$S$_8$, GaV$_4$Se$_8$ [12,17–22], and GaMo$_4$S$_8$ [23]. These materials crystallize in the cubic lacunar spinel structure [24–31], which becomes polar below ∼45 K and the point symmetry is reduced from T_d to C_{3v} [17,31–33]. Since the magnetic order develops in the polar phase, these compounds are multiferroic. Furthermore, the skyrmions posses a nontrivial electric polarization pattern due to the magnetoelectric effect [31], which may enable nearly dissipation free manipulation of the magnetic order by electric fields [32].

In addition to obvious differences in the spin texture of Bloch- and Néel-type skyrmions, the phase diagrams of cubic helimagnets and polar skyrmion hosts are markedly different. In cubic helimagnets, the term in the magnetic energy corresponding to the DMI has an isotropic form: $w_{DMI} = \mathbf{M} \cdot (\nabla \times \mathbf{M})$. Therefore, the plane of the SkL aligns itself to be nearly perpendicular to the applied magnetic field, irrespective of the field's direction. This isotropic interaction also results in a narrow stability range of for Bloch-type skyrmions in the vicinity of the magnetic ordering temperature due to competition with the longitudinal conical phase [1,15]. In contrast, C_{nv} ($n \geqslant 3$) symmetry only allows an axially symmetric DMI interaction. Therefore, in polar skyrmion hosts, modulated magnetic structures with wave vectors perpendicular to the high symmetry, polar axis are favored. In these compounds, the orientation of Néel skyrmions is locked to

the polar axis rather than the applied magnetic field. Thus, instead of tilting the plane of the SkL, oblique applied fields distort the configuration of the Néel skyrmions and displace their cores [34]. This property has two consequences on the magnetic phase diagram of such materials: (1) the SkL phase is more robust than in cubic helimagnets because the conical phase is suppressed, and (2) its stability range depends on the direction of the applied field. In addition, the second-order magnetic anisotropy allowed in this symmetry can also modify the phase diagram. In the case of GaV_4S_8, strong easy-axis anisotropy [33] suppresses the modulated phases at low temperature [19], whereas in GaV_4Se_8 easy-plane anisotropy helps to stabilize the SkL phase down to the lowest temperatures [12,18,20].

Here, we use dynamic cantilever magnetometry (DCM) [35–37] to map the magnetic phase boundaries in GaV_4S_8 and GaV_4Se_8 as a function of the strength and orientation of magnetic field. We determine the corresponding phase diagrams, which reproduce the major features predicted by a recent theoretical model [34]. The measurements constitute a direct experimental confirmation of the robustness of Néel-type skyrmions to oblique magnetic fields in two materials with uniaxial magnetic anisotropy of opposite signs. In addition to magnetic transitions between the cycloidal, SkL, and field-polarized ferromagnetic states, in GaV_4Se_8, we also observe sharp anomalies in the torque, which we assign to field-driven transformations of magnetic states confined to polar domain walls (DWs).

II. DYNAMIC CANTILEVER MAGNETOMETRY

In DCM, the sample under investigation is attached to the end of a cantilever, which is driven into self-oscillation at its resonance frequency f. Changes in this resonance frequency $\Delta f = f - f_0$ are measured as a function of the uniform applied magnetic field $\mathbf{H}$, where f_0 is the resonance frequency at $H = 0$. Δf reveals the curvature of the magnetic energy E_m with respect to rotations about the cantilever oscillation axis [35,36]:

$$\Delta f = \frac{f_0}{2k_0 l_e^2} \left(\frac{\partial^2 E_m}{\partial \theta_c^2} \bigg|_{\theta_c=0} \right), \tag{1}$$

where k_0 is the cantilever's spring constant, l_e its effective length, and θ_c its angle of oscillation. Measurements of this magnetic curvature are particularly useful for identifying magnetic phase transitions [35] since—just as the magnetic susceptibility—it should be discontinuous for both first- and second-order phase transitions [38].

DCM measurements are carried out in a vibration-isolated closed-cycle cryostat. The pressure in the sample chamber is less than 10^{-6} mbar and the temperature can be stabilized between 4 and 300 K. Using an external rotatable superconducting magnet, magnetic fields up to 4.5 T can be applied along any direction spanning $120°$ in the plane of cantilever oscillation, as shown in Fig. 1. $\hat{\mathbf{x}}$ in our coordinate system is defined by the cantilever's long axis, while $\hat{\mathbf{y}}$ coincides with its axis of oscillation. β is the angle between $\mathbf{H}$ and $\hat{\mathbf{x}}$ in the xz-plane. The cantilever's motion is read out using a optical fiber interferometer using 100 nW of laser light at 1550 nm [39]. A piezoelectric actuator mechanically drives
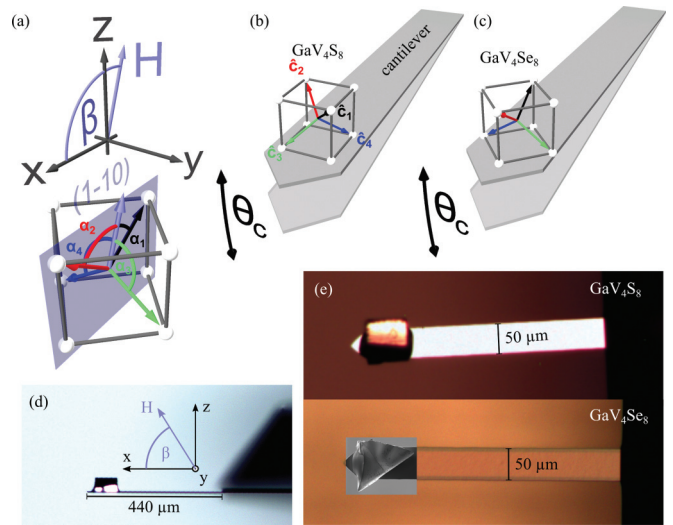

FIG. 1. Schematics of the measurement setup. (a) The coordinate system and the definition of β as the angle between $\mathbf{H}$ and $\hat{\mathbf{x}}$ in the top figure. Below, the rotation plane of $\mathbf{H}$ and the definition of the angles α_i is given. (b), (c) The cantilever, its oscillation angle θ_c, and the crystalline axes of the measured samples. Black, red, green, and blue lines correspond to the four $\hat{\mathbf{c}}_i$. (d) The orientation of $\mathbf{H}$ with respect to an optical image of a sample and cantilever. (e) Composite optical and scanning electron micrographs of the measured GaV_4S_8 and GaV_4Se_8 samples mounted on their respective cantilevers.

the cantilever at f with a constant oscillation amplitude of a few tens of nanometers (corresponding to oscillation angles of tens of microradians) using a feedback loop implemented by a field-programmable gate array. This process enables the fast and accurate extraction of f from the cantilever deflection signal as well as providing a measure of the dissipation Γ, which described the system's rate of energy loss: $dE/dt = -\Gamma l_e^2 \dot{\theta}_c^2$. To maintain a constant oscillation amplitude, the cantilever must be driven with a force $F = \Gamma l_e \dot{\theta}_c$, such that any losses due to dissipation are compensated. The voltage amplitude used to drive the piezoelectric actuator is therefore proportional to $\Gamma = \Gamma_0 + \Gamma_m$ where Γ_0 is the cantilever's intrinsic mechanical dissipation at $H = 0$ and Γ_m represents magnetic losses. Given that Γ_m reflects the sample's magnetic relaxation, Γ should undergo abrupt changes at magnetic phase transitions. We therefore use both measurements of the magnetic curvature and dissipation, combined with knowledge from other measurements [12,17–20], to map the low-temperature magnetic phase diagrams of GaV_4S_8 and GaV_4Se_8 as a function of $\mathbf{H}$.

III. SAMPLES

Single crystals of GaV_4S_8 and GaV_4Se_8 are grown by a chemical transport reaction method using iodine as a transport agent [17]. X-ray diffraction measurements of both sample materials show impurity-free single-crystals [31]. For the DCM measurement, we attach individual crystals of GaV_4S_8 and GaV_4Se_8, which are a few tens of micrometers in size, to the ends of commercial Si cantilevers (Nanosensors™TL-cont) using nonmagnetic epoxy, as shown in Fig. 1. These
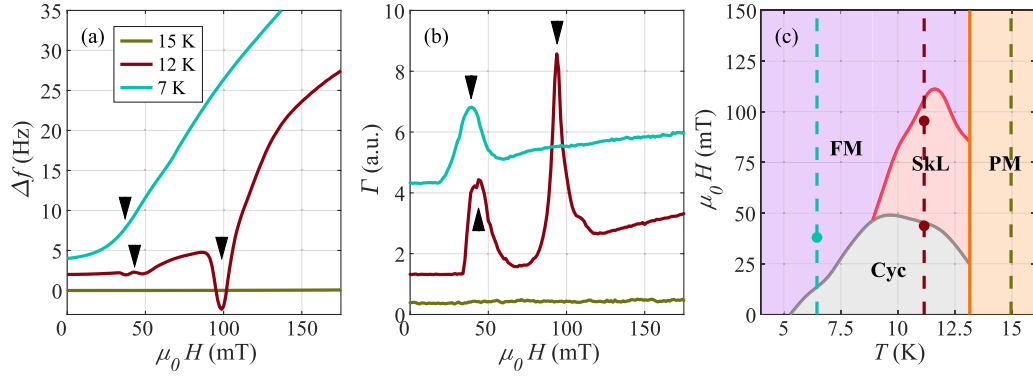
FIG. 2. Temperature and field dependence of magnetic phase transitions measured by DCM in GaV_4S_8. DCM measurements of (a) $\Delta f(H)$ and (b) $\Gamma(H)$ taken at $T = 7$, 12, and 15 K in cyan, maroon, and brown, respectively. Curves are shifted for better visibility. $\beta = 0$, i.e., approximately **H** ∥ [100]. Arrows indicate features corresponding to phase transitions. (c) Sketch of the expected magnetic phase diagram as a function of temperature and applied field for **H** ∥ [100] [17]. Color-coded dashed lines and points correspond to temperatures and measured features in (a) and (b).

cantilevers are 440-μm-long, 50-μm-wide, and 2.3-μm-thick. Unloaded, they have resonance frequencies of about 16 kHz, quality factors around 5×10^5, and spring constants of 300 mN/m. Due to the additional mass of the samples, the resonance frequency of a loaded cantilever shifts to around 3 kHz.

Both samples are attached near the free end of the cantilever with the (001) surface pressed flat against the Si surface. The orientation of the GaV_4S_8 and GaV_4Se_8 samples differs and can be roughly estimated from optical and scanning electron microscope images. The resultant direction of each sample's crystalline axes with respect to the cantilever is shown in Fig. 1: specifically the approximate orientation of the four cubic $\langle 111 \rangle$ axes $\hat{\mathbf{c}}_\mathbf{i}(i = 1, 2, 3, 4)$ is shown in black, red, green, and blue.

Both GaV_4S_8 and GaV_4Se_8 undergo a Jahn-Teller structural phase transition from a noncentrosymmetric cubic to a rhombohedral structure at 44 and 42 K, respectively [11,12,30,31]. The transition is characterized by a stretching of the cubic unit cell along one of the four cubic body diagonals $\hat{\mathbf{c}}_\mathbf{i}$, resulting in four different structural domains. The rhombohedral distortion also gives rise to polarization along $\hat{\mathbf{c}}_\mathbf{i}$, making these the polar axes of the system. The multidomain state is composed of sub-micrometer-thick sheets of these four different rhombohedral polar domains, which we label P_i [20,21]. The polar axis $\hat{\mathbf{c}}_\mathbf{i}$ also corresponds to the axis of magnetic anisotropy in the respective rhombohedral domain state. In GaV_4S_8, the uniaxial anisotropy is of easy-axis type, while in GaV_4Se_8 it is of easy-plane type [17,18,33]. In both materials, measurements indicate the presence of modulated magnetic phases including a cycloidal (Cyc) state, a Néel-type SkL, and a field-polarized ferromagnetic (FM) phase [17,18]. The population of multiple rhombohedral domains at low temperature complicates the determination of the magnetic phase diagram because, for any given orientation of the applied field **H**, there can be up to four different angles, α_i, between **H** and $\hat{\mathbf{c}}_\mathbf{i}$ as shown in Fig. 1(a). Note that we define α_i modulo 180°; due to crystal symmetry, if α_i exceeds 180°, the relevant angle is between **H** and $-\hat{\mathbf{c}}_\mathbf{i}$. As a result of the four possible α_i, for an arbitrary orientation of **H**, a single phase transition can appear at up to four different values of H, depending on the projections of **H** on each $\hat{\mathbf{c}}_\mathbf{i}$. Although the application of a large electric field upon cooling through the structural phase transition has been
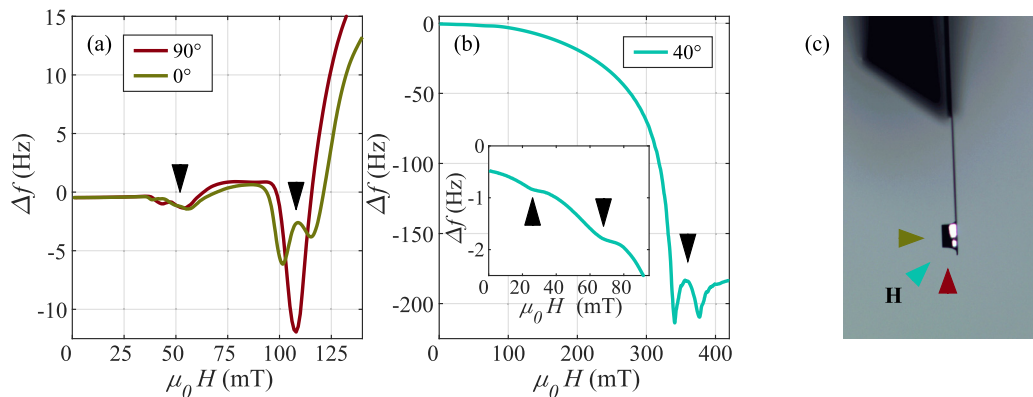

FIG. 3. Angular dependence of magnetic phase transitions measured by DCM in GaV_4S_8. (a), (b) $\Delta f(H)$ at $T = 11$ K for at $\beta = 0$, 40, and 90° in maroon, cyan, and brown, respectively. Arrows indicate features corresponding to phase transitions. Inset: Zoomed view of the low-field region. (c) Schematic diagram showing the three measured orientations relative to the sample-loaded cantilever.

shown to polarize GaV_4S_8 and GaV_4Se_8 samples such that only a single domain is populated [11,12], it is practically challenging to apply such fields in a DCM apparatus.

IV. MEASUREMENTS

A. GaV_4S_8

Figure 2 shows DCM measurements of $\Delta f(H)$ and $\Gamma(H)$ in GaV_4S_8 for different temperatures T. The data shown in Figs. 2(a) and 2(b) are collected with **H** aligned along the cantilever's long axis ($\beta = 0$), i.e., approximately **H** ∥ [100]. In this configuration, the angles α_i between **H** and the four $\hat{c}_i$ are the same within the precision of the sample orientation, i.e., within a few degrees. Consequently, each magnetic phase transition should occur at a similar value of H for each domain. In this particularly simple case, we compare $\Delta f(H)$ and $\Gamma(H)$ at different temperatures to the corresponding magnetic phase diagram measured by Kézsmárki *et al.* [17] and shown schematically in Fig. 2(c). Where metamagnetic transitions are expected, they manifest themselves as dips in $\Delta f(H)$ and peaks in $\Gamma(H)$. At $T = 12$ K, the two features at 45 and 100 mT (indicated by arrows) correspond to the Cyc-to-SkL and the SkL-to-FM phase transitions, respectively. The double dip (peak) feature in $\Delta f(H)$ [$\Gamma(H)$] comes from the imperfect alignment of the sample's crystalline axes with the coordinate system of our measurement setup, resulting in a difference in α_i for each domain. At $T = 7$ K only one feature is found, corresponding to the Cyc-to-FM transition, while at $T = 15$ K, which is above the magnetic ordering temperature, no features are observed.

H is rotated approximately in the (010) plane such that, in general, by changing β, we change each α_i differently. As a result, the number of features related to phase transitions and the fields at which they occur can also change. The dependence that we observe is consistent with the orientation of our sample and previous measurements by Kézsmárki *et al.* In particular, we note that, because of the crystal's alignment and its cubic symmetry, the measured curves should repeat themselves upon rotating β by 90°. This periodic behavior can be seen in Fig. 3(a), where two DCM curves with $\beta = 0$ and 90° nearly overlap; differences, including the splitting of the dips in $\Delta f(H)$ into two dips, are again related to the slight misalignment of the sample's crystalline axes with respect to the applied field, resulting in slightly different α_i for each domain. In the curve taken with $\beta = 40°$ (approximately **H** ∥ [101]) shown in Fig. 3(b), we observe four features. The features observed at 26 and 68 mT are the Cyc-to-SkL and the SkL-to-FM phase transitions, respectively, also observed by Kézsmárki *et al.* These transitions correspond to the P_4 and P_1 domains (blue and black in Fig. 1) with $\alpha_4 = 31.7°$ and $\alpha_1 = 39.2°$. The two transitions at 320 and 370 mT correspond to the Cyc-to-FM transitions in the P_3 and P_2 domains (green and red in Fig. 1), where $\alpha_3 = 84.5°$ and $\alpha_2 = 88.8°$. As before, the mismatches $\alpha_4 \neq \alpha_1$ and $\alpha_3 \neq \alpha_2$ and the resulting pair of split features are due to the crystal's imperfect alignment with the applied field.

Using the measured features in $\Delta f(H)$ and $\Gamma(H)$, we map the magnetic phase transitions of GaV_4S_8 as a function of H and β. After initializing the system with a large external field
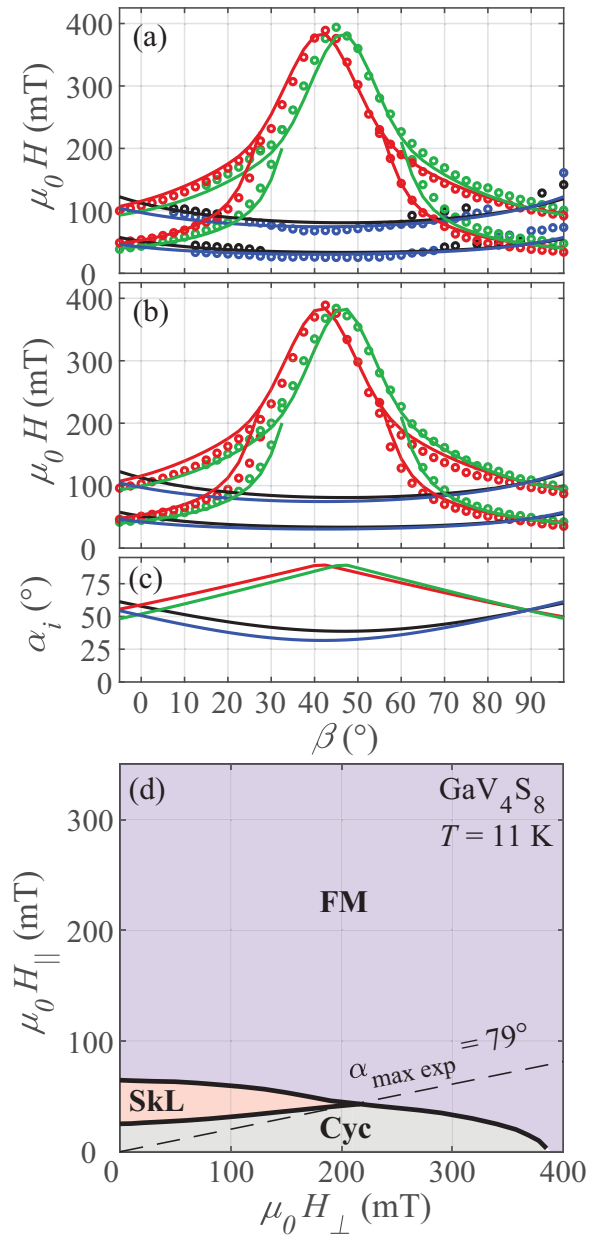

FIG. 4. Magnetic phase transitions measured in GaV_4S_8 at $T = 11$ K. Features extracted from DCM measurement of (a) $\Delta f(H)$ and (b) $\Gamma(H)$ are plotted as open circles as a function of β. Black, red, green, and blue circles correspond to domains P_1, P_2, P_3, and P_4, respectively. Color-coded lines indicate phase boundaries for each domain according to the phase diagram in (d). (c) Angle α_i between the corresponding $\hat{c}_i$ and the external field **H** vs β for all four rhombohedral domains, using the same color code as in (a) and (b). (d) Best-fit magnetic phase diagram for single-domain GaV_4S_8 as a function of field applied perpendicular and parallel to the axis of symmetry.

$H = 1$ T, DCM measurements are made by stepping H toward zero at a fixed β and T. The angular dependence over the range $-5° < \beta < 100°$ is recorded at $T = 11$ K by changing β in steps of 2.5° and repeating the measurement. We plot the features identified in these measurements as open circles in Figs. 4(a) and 4(b). By comparing our data taken for a
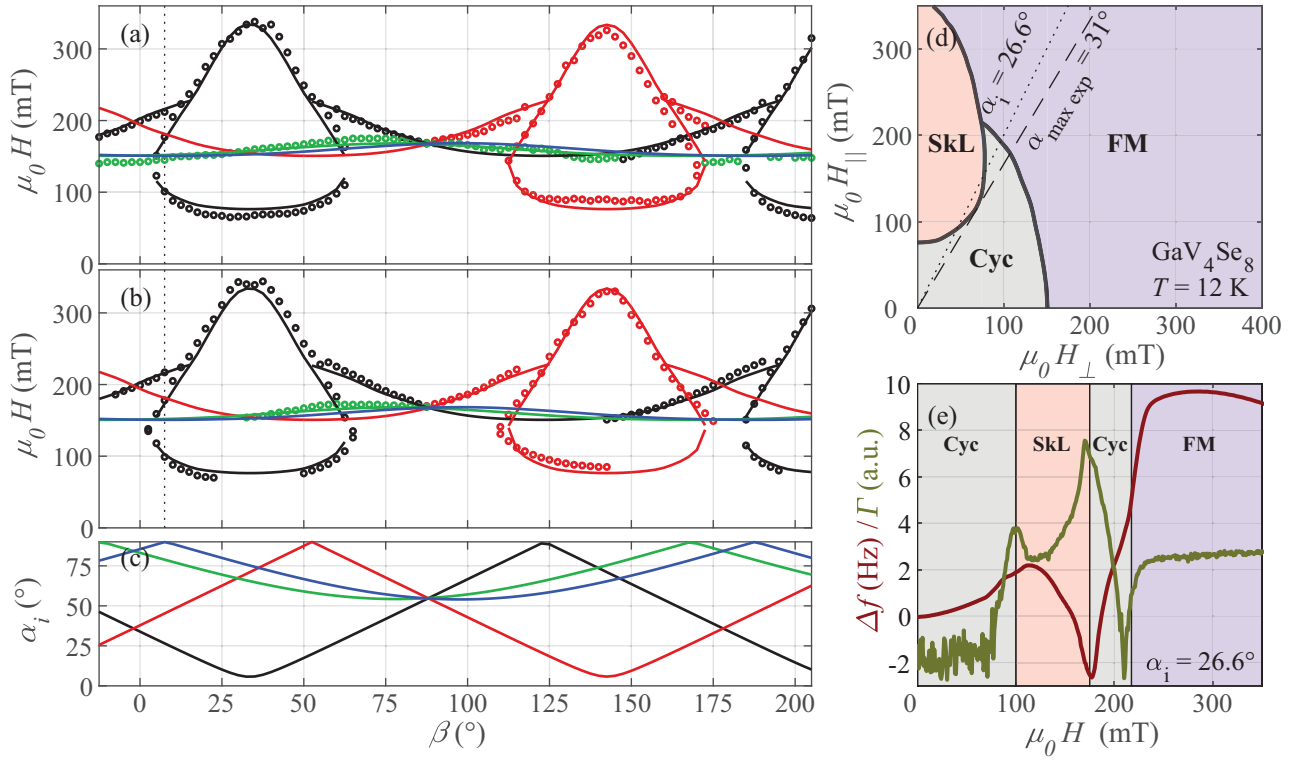
FIG. 5. Magnetic phase transitions measured in GaV$_4$Se$_8$ at $T = 12$ K. Transitions extracted from DCM measurement of (a) $\Delta f(H)$ and (b) $\Gamma(H)$ are plotted as open circles as a function of β. Black, red, green, and blue circles correspond to transitions for domain P_1, P_2, P_3, and P_4, respectively. Color-coded lines correspond to phase boundaries for the each color-coded domain as indicated by lines in the phase diagram (d). (c) Angle α_i between corresponding polar axis and the external field **H** vs β for all four rhombohedral domains, using the same color code as in (a) and (b). (d) Best-fit magnetic phase diagram for single-domain GaV$_4$Se$_8$ as a function of field applied perpendicular and parallel to the axis of symmetry. (e) DCM measurement of $\Delta f(H)$ for $\alpha_i = 26.6°$ ($\beta = 7.5°$) showing the reentrant Cyc phase of domain 1 (black). Transitions from other domains are not indicated. These measurements corresponds to line-cuts along the dotted vertical lines in (a) and (b) and the dotted diagonal line labeled $\alpha_i = 26.6°$ in (d).

few magnetic field orientations to the phase diagram reported by Kézsmárki *et al.* [17], we assign each feature to a certain type of transition (i.e., Cyc-to-FM, Cyc-to-SkL, SkL-to-FM) occurring in a certain domain state (P_1, P_2, P_3, P_4).

Next, we determine the dependence of the phase boundaries on the orientation of the magnetic field with respect to the axis of the uniaxial magnetic anisotropy. The measured signatures shown as open circles in Figs. 4(a) and 4(b) can be fit by assuming that each of the four rhombohedral domains of GaV$_4$S$_8$ obeys the magnetic phase diagram shown in Fig. 4(d), plotted as a function of $H_\parallel$ and $H_\perp$, the components of **H** parallel and perpendicular to the rhombohedral axis $\hat{\mathbf{c}}_\mathbf{i}$, respectively. A feature in Δf and Γ observed at certain H and β corresponds to a transition of a particular domain P_i for a field of magnitude H and angle α_i with respect to $\hat{\mathbf{c}}_\mathbf{i}$, as shown in Fig. 4(c). The magnitude H and the angle α_i at which each feature occurs, correspond to a point on a phase boundary in the diagram of Fig. 4(d), through $H_\parallel = H \cos \alpha_i$ and $H_\perp = H \sin \alpha_i$. This phase diagram reflects the general form suggested by Leonov and Kézsmárki [34]. Phase boundaries corresponding to the diagram are also plotted as a function of β and H in Figs. 4(a) and 4(b) to show their agreement with the measurements. They appear as solid lines, which are color-coded according to the domain to which they belong. A Euler rotation of the crystal (-5.0, 0.2 and $10.0°$) with respect

to ideal configuration, shown in Fig. 1(b), is required such that the phase boundaries corresponding to the different domain states collapse onto the single boundary diagram of Fig. 4(d). Note that features shown in Figs. 4(a) and 4(b) related to the Cyc-to-FM transitions of P_1 (black) and P_4 (blue) are very weak in $\Delta f(H)$ and not observable in $\Gamma(H)$. Given that we cannot control the population of the domains, it is likely that the sample is in a multidomain state dominated by P_2 (red) and P_3 (green) domains.

The agreement between the measured features and fit phase boundaries allows us to eliminate complications arising from the multidomain nature of the crystal and, thus, to extract a the general magnetic phase diagram of GaV$_4$S$_8$ as a function of the field applied parallel and perpendicular to the anisotropy axis. The position of the intersection between the different phase transitions in Fig. 4(d) shows that the SkL phase in GaV$_4$S$_8$ persists in oblique fields up to a threshold angle as large as $\alpha_{max} = 79°$. For larger α, the cycloidal state directly transforms to the ferromagnetic state upon increasing H. The extent of the SkL phase shows stronger stability against fields applied perpendicular to the anisotropy axis (up to $H_\perp = 200$ mT) than fields applied parallel (up to $H_\parallel = 65$ mT). The critical angle α_{max} is larger than predicted by Leonov and Kézsmárki [34], although their model was not designed for strict quantitative comparisons.
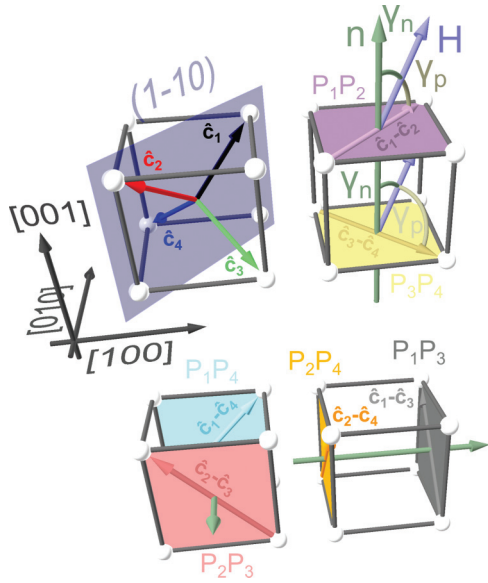
FIG. 6. Schematic for understanding the orientation of the 6 different domain walls types. Top left: Directions of the four possible polar axes, P_1-P_4, which are the axes of magnetic anisotropy within the corresponding domains. The transparent blue plane indicates the approximate plane of rotation of the external magnetic field. Top right: Mechanically compatible and charge neutral DWs separating P_1 and P_2 domains are parallel to the (001) plane, just as DWs between P_3 and P_4 domains. The former and latter DWs are referred to as P_1P_2 and P_3P_4, respectively. γ_n, the angle between **H** and the normal vector **n**, which is proportional to $\hat{\mathbf{c}}_i + \hat{\mathbf{c}}_j$, is shown for both DW pairs. γ_p, the angle between **H** and $\hat{\mathbf{c}}_i - \hat{\mathbf{c}}_j$, is also shown. Bottom: The other two pairs of DWs sharing the same orientation. The normal vector of the corresponding planes and their labels are indicated for the three cases, as well as the difference vector $\hat{\mathbf{c}}_i - \hat{\mathbf{c}}_j$, unique to each DW type.

B. GaV$_4$Se$_8$

We apply the same experimental procedure to explore the magnetic phase diagram of GaV$_4$Se$_8$. In this case, **H** is rotated approximately in the (1$\bar{1}$0) plane. Figs. 5(a) and 5(b) show the angular dependence of the features, as extracted from measurements of $\Delta f(H)$ and $\Gamma(H)$ at $T = 12$ K. Using previous measurements made by Bordács *et al.* along particular crystalline directions [18], as well as neutron diffraction data by Geirhos *et al.* [20] for guidance, we assign each feature to a transition between Cyc, SkL, or FM states for a certain domain and color-code it accordingly.

Once again, the measured features are shown as open circles in Figs. 5(a) and 5(b) and can be fit by assuming that each of the four rhombohedral domains obeys a single magnetic phase diagram shown in Fig. 5(d). The magnitude of the applied field H and its angle α_i with respect to the assigned domain's rhombohedral axis $\hat{\mathbf{c}}_i$ put each feature on one of the phase boundaries depicted in Fig. 5(d). Phase boundaries corresponding to the phase diagram are plotted in Figs. 5(a) and 5(b) for comparison to the measured data. They appear as solid lines, which are color-coded according to the domain. Similarly to GaV$_4$S$_8$, the overall form of the phase diagram agrees with that suggested by Leonov and Kézsmárki [34].

Note that the rotation plane of **H**, approximately (1$\bar{1}$0), contains $\hat{\mathbf{c}}_1$ and $\hat{\mathbf{c}}_2$, but not $\hat{\mathbf{c}}_3$ and $\hat{\mathbf{c}}_4$. A Euler rotation of the crystal (-14, -1, and $7°$) with respect to the ideal configuration, shown in Fig. 1(c), is required such that the phase boundaries corresponding to the different domain states (P_1, P_2, P_3, P_4) collapse onto the single boundary diagram of Fig. 5(d). We find additional anomalies in both $\Delta f(H)$ and $\Gamma(H)$ that cannot be ascribed to the boundaries between the Cyc, SkL, and FM phases. We suspect that these anomalies originate from the formation of magnetic textures localized at structural DWs, as discussed in Sec. IV C.

Features assigned to the Cyc-to-FM transition of domain P_3 (green) are difficult to distinguish from those occuring for the same transition in P_4 (blue) because they are expected to occur at nearly the same H and β in Figs. 5(a) and 5(b). Since this distinction does not affect the form of the phase diagram in Fig. 5(d), our assignment of all such features to the P_3 rather than P_4 transition is unimportant. For the P_1 (black) and P_2 (red) domains, which are the only two experiencing sufficient $H_\parallel$ to reach the SkL phase, the boundaries of the SkL state appear as prominent rain-drop-like shapes in Figs. 5(a) and 5(b). From the intersection of the SkL with the Cyc phase boundary in Fig. 5(d), we extract a threshold angle $\alpha_{\max} = 31°$ for the SkL phase in GaV$_4$Se$_8$ at $T = 12$ K. Contrary to GaV$_4$S$_8$, the extent of the SkL phase shows stronger stability against fields applied parallel to the anisotropy axis (up to $H_\parallel = 340$ mT) than fields applied perpendicular (up to $H_\perp = 75$ mT). Furthermore, we note the presence of a reentrant Cyc phase for angles $19° < \alpha_i < 30°$, as predicted by Leonov and Kézsmárki [34]. For this range of α_i, two successive first-order phase transitions from Cyc to SkL and back occur as a function of increasing field. The signature of this behavior in DCM is shown in Fig. 5(e).

C. Magnetic states confined to domain walls in GaV$_4$Se$_8$

Geirhos *et al.* observed anomalies in various macroscopic thermodynamic properties of GaV$_4$Se$_8$, emerging exclusively in crystals with polar multidomain structure. They suggest a possible scenario for the formation of magnetic states at the structural DWs [20]. Magnetic interactions change stepwise at the DWs, where spin textures with different spiral planes, hosted by neighboring domains, need to be matched. This can, for example, lead to conical magnetic states at the DWs with a different closing field magnitude than bulk magnetic states. Here, we adopt and modify this model in order to analyze its applicability to anomalies observed in our DCM measurements of GaV$_4$Se$_8$, which cannot be assigned to bulk magnetic phase transitions.

In the rhombohedral phase of the studied lacunar spinels, mechanically compatible and charge-neutral DWs are normal to $\hat{\mathbf{c}}_i + \hat{\mathbf{c}}_j$, the sum of the two polar directions of the domain states P_i and P_j separated by the DW, as shown in Fig. 6 [20,21,40]. For example, mechanically and electrically compatible DWs connecting a P_1 (black) and a P_2 (red) domain are parallel to (001) planes, cf., Fig. 6. The same is true for DWs between P_3 (green) and P_4 (blue) domains.

For an arbitrary orientation of the external magnetic field, magnetic states confined to DWs with different orientations are expected to undergo field-induced transitions, similarly to
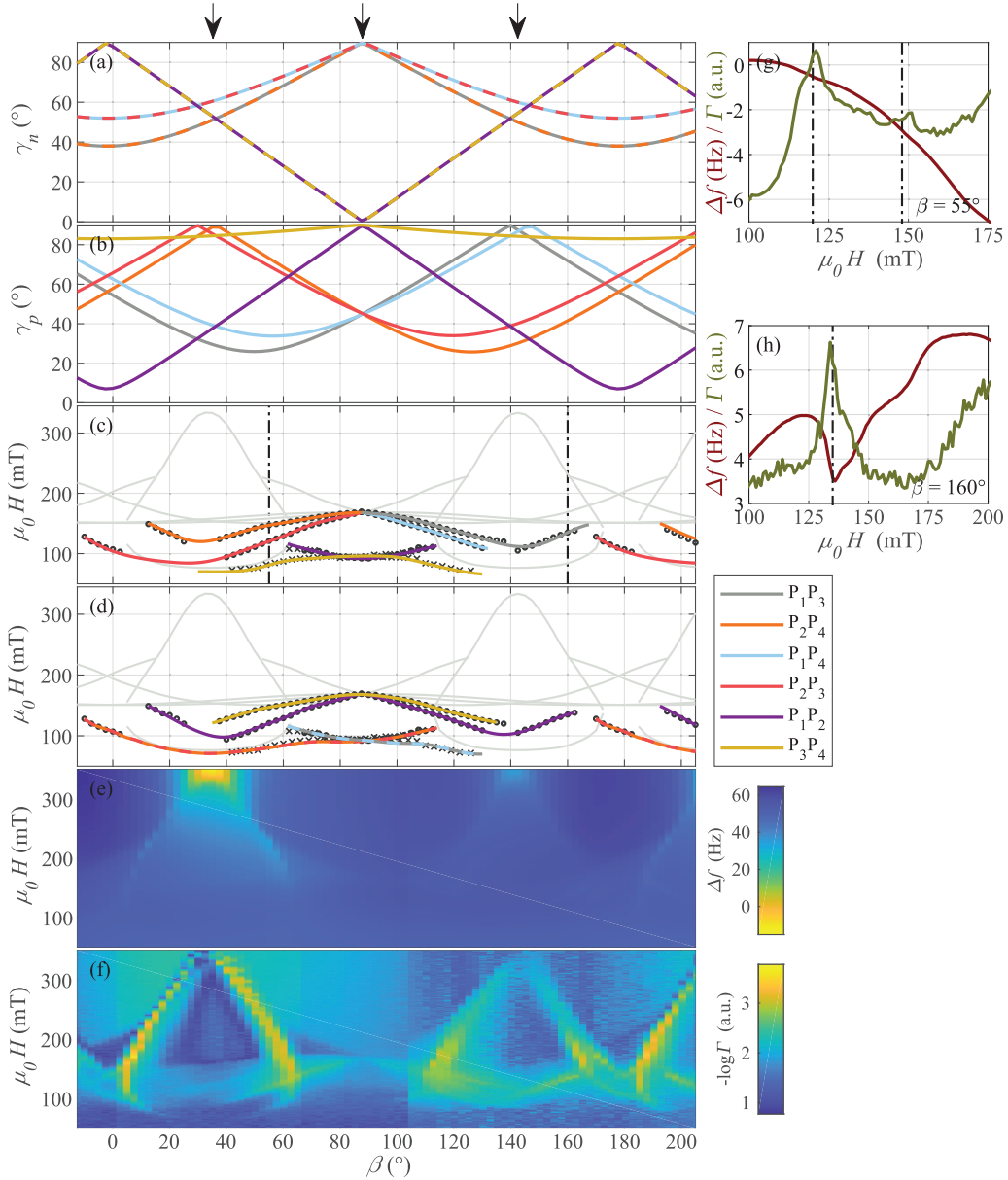
FIG. 7. Anomalies in $\Delta f(H)$ and $\Gamma(H)$ assigned to transitions of DW rather than bulk magnetic states. Arrows at the top indicate from left to right the approximate angle β corresponding to the [111], [001], and [11 − 1] directions, respectively. (a) Angle γ_n between the normal vector of a DW and **H** plotted against β. The color of the dashed lines shows their correspondence to a DW type in the legend. (b) Angle γ_p between the vector formed by the difference of the polar axis vectors of the two adjacent domains of a DW and **H** plotted against β. (c) Transitions extracted from both Δf and Γ that are not assigned to a domain transition (circles). Crosses show transitions extracted from magnetoelectric measurements [20], scaled by about 0.9 to match the DCM data. Colored lines show the suggested assignment of the transitions to DW types as denoted in the legend. Light gray lines show the bulk domain transitions. (d) Same data as in (c) with a different assignment of transitions. Color map of (e) $\Delta f(H, \beta)$ and (f) $-\log_{10} \Gamma(H, \beta)$. (g), (h) Example DCM measurements with dash-dotted vertical lines indicating the assigned transition fields. Dash-dotted vertical lines in (c) indicate the value of β of the example measurements.

the bulk (in-domain) magnetic states. However, in this case the situation is more complex: The stability of the magnetic states confined to DWs is determined by the orientation of the field with respect to the magnetic anisotropy axes of adjacent domains and to the DW itself.

It is reasonable to assume that the angle γ_n between **H** and the normal of the DW planes, given by $\hat{\mathbf{c}}_i + \hat{\mathbf{c}}_j$, plays a decisive role in setting the angular range, across which confined states are stable. This leads to three pairs of DWs, as shown

in Fig. 6, each sharing the same γ_n for a given **H**. For DWs in a pair, however, the relative orientation between the magnetic anisotropy axes of the two domains involved and **H** is not the same. For example, consider the P_1P_2/P_3P_4 pair: the rotation plane of **H** $(1\bar{1}0)$ contains the anisotropy axes of P_1 and P_2, but not the anisotropy axes of P_3 and P_4; they span 54° with this plane. We therefore introduce another angle γ_p between **H** and the difference of the two polar vectors $\hat{\mathbf{c}}_i - \hat{\mathbf{c}}_j$, which lies in the DW plane. Both these angles $\gamma_n(\beta)$ and $\gamma_p(\beta)$, plotted

in Figs. 7(a) and 7(b), respectively, are expected to affect the stability of the DW-confined magnetic states.

In the angular dependent torque measurements, shown in Figs. 7(c) to 7(f), we observe at most four anomalies (open circles) for a given field orientation. Since there are six types of DWs, distinguished by γ_n and γ_p, some transitions, which occur simultaneously in different types of DWs appear as a single anomaly, while some transitions appear not to be experimentally observable. In the following analysis, we take into account an additional anomaly (crosses) between $\beta \simeq 40$ and $130°$ at field values around 100 mT, which is not present in our DCM measurements, but has been observed in magnetoelectric measurements [20]. Example measurements of Δf and Γ are shown in Figs. 7(g) and 7(h), where anomalies assigned to DW states are indicated by vertical dash-dotted lines.

As a first scenario, we suggest the assignment of the observed anomalies as shown in Fig. 7(c). In this way, both domains adjacent to a DW host the Cyc state and the DW-confined state emerges due to the matching of these two cycloidal patterns for all observed anomalies. This is specifically notable for the anomalies meeting at $\beta \approx 90°$. For example, the anomaly assigned to be a P_2P_4 DW (orange), would progress above 150 mT for $\beta > 90°$, but because in-domain states within the P_4 domain (blue axis) transform from the Cyc to the FM state for $\beta > 90°$ and $H > 150$ mT, this anomaly disappears for larger angles. The same is true for the other end of this anomaly ($\beta = 12.5°$). Similarly, the anomalies assigned to transitions in the P_1P_2 DWs are limited by the two skyrmion pockets of the P_1 and P_2 domains. No anomaly is observed in angular ranges, where the adjacent domains host magnetic states other than the Cyc.

An alternative scenario is an extension of the one suggested by Geirhos *et al.* [20], shown in Fig. 7(d). This scenario allows some DW transitions to persist even when one of the adjacent domains is in the Cyc phase, while the other one is in the SkL phase. Such a situation occurs for the P_1P_2 DW transition, which penetrates both the P_1 and the P_2 SkL pockets.

In both scenarios, the mirror symmetry expected across $\beta \simeq 90°$, as dictated by $\gamma_n(\beta)$ and $\gamma_p(\beta)$ is fulfilled: the transition lines are either symmetric to this point or they have a symmetry-related counterpart. The basis for both scenarios is the occurrence of a distinct magnetic state confined to DWs, and its transition to the FM state at certain critical field, observed as an additional anomaly in the DCM measurement. The angle of the applied field with the DW-normal, γ_n, and the orientation of its component in the DW-plane, γ_p, appear to be a important parameters in determining the critical field of the DW states.

V. CONCLUSION

We extract magnetic phase diagrams as a function applied field magnitude and direction for both GaV_4S_8 and GaV_4Se_8 that are in good qualitative agreement with the

theoretical predictions of Leonov and Kézsmárki [34], confirming the general validity of their model. This agreement, in turn, provides indirect confirmation that, under oblique applied magnetic field, the axes of Néel-type skyrmions stay locked to the anisotropy axis while their structure distorts and their core displaces. The measurements reproduce the overall structure of the phase diagrams, imposing a maximum angle α_{max} of magnetic field applied with respect to the anisotropy axis, for which a SkL phase persists. In addition, they show that easy-axis anisotropy—as found in GaV_4S_8—enhances the robustness of Néel skyrmions against magnetic fields applied perpendicular to the symmetry axis, while easy-plane anisotropy—as found in GaV_4Se_8—increases their stability for fields parallel to this axis. Our results also confirm the existence of a reentrant Cyc phase in GaV_4Se_8, which was anticipated to occur for certain values of easy-plane anisotropy. Finally, anomalies in $\Delta f(H)$ and $\Gamma(H)$, which cannot be explained as bulk domain transitions, are consistent with distinct magnetic states confined to polar structural DWs and their transition from the Cyc to FM state, as proposed by Geirhos *et al.* [20].

Nevertheless, the measured magnetic phase diagrams are not in strict quantitative agreement with the predicted ones. For GaV_4S_8, we are unable to tune the uniaxial anisotropy of the model to match the measured values of threshold angle of the SkL phase $\alpha_{max} = 79°$ at $T = 11$ K. This discrepancy suggests that approximations made in the model ignore important details, thus preventing it from capturing the full behavior of the system. Possible improvements to the model include consideration of the anisotropic exchange interaction, an extension from two to three dimensions, or the consideration of metatable magnetic states. Also, further experimental investigation—especially real-space imaging—of anomalies assigned to transitions of DW-confined magnetic states is required to characterize the spin pattern associated with these states.

[1] S. Mühlbauer, B. Binz, F. Jonietz, C. Pfleiderer, A. Rosch, A. Neubauer, R. Georgii, and P. Böni, Science **323**, 915 (2009).

[2] A. N. Bogdanov and D. A. Yablonskii, Zh. Eksp. Teor. Fiz. **95**, 178 (1989) [Sov. Phys. JETP **68**, 101 (1989)].

[3] A. Bogdanov and A. Hubert, J. Magn. Magn. Mater. **138**, 255 (1994).

[4] X. Z. Yu, Y. Onose, N. Kanazawa, J. H. Park, J. H. Han, Y. Matsui, N. Nagaosa, and Y. Tokura, Nature **465**, 901 (2010).

[5] X. Z. Yu, N. Kanazawa, Y. Onose, K. Kimoto, W. Z. Zhang, S. Ishiwata, Y. Matsui, and Y. Tokura, Nat. Mater. **10**, 106 (2011).

[6] H. Du, R. Che, L. Kong, X. Zhao, C. Jin, C. Wang, J. Yang, W. Ning, R. Li, C. Jin, X. Chen, J. Zang, Y. Zhang, and M. Tian, Nat. Commun. **6**, 8504 (2015).

[7] Y. Tokunaga, X. Z. Yu, J. S. White, H. M. Rønnow, D. Morikawa, Y. Taguchi, and Y. Tokura, Nat. Commun. **6**, 7638 (2015).

[8] T. Schulz, R. Ritz, A. Bauer, M. Halder, M. Wagner, C. Franz, C. Pfleiderer, K. Everschor, M. Garst, and A. Rosch, Nat. Phys. **8**, 301 (2012).

[9] F. Jonietz, S. Mühlbauer, C. Pfleiderer, A. Neubauer, W. Münzer, A. Bauer, T. Adams, R. Georgii, P. Böni, R. A. Duine, K. Everschor, M. Garst, and A. Rosch, Science **330**, 1648 (2010).

[10] P.-J. Hsu, A. Kubetzka, A. Finco, N. Romming, K. V. Bergmann, and R. Wiesendanger, Nat. Nanotechnol. **12**, 123 (2017).

[11] E. Ruff, A. Butykai, K. Geirhos, S. Widmann, V. Tsurkan, E. Stefanet, I. Kézsmárki, A. Loidl, and P. Lunkenheimer, Phys. Rev. B **96**, 165119 (2017).

[12] Y. Fujima, N. Abe, Y. Tokunaga, and T. Arima, Phys. Rev. B **95**, 180410(R) (2017).

[13] J. Sampaio, V. Cros, S. Rohart, A. Thiaville, and A. Fert, Nat. Nanotechnol. **8**, 839 (2013).

[14] R. Tomasello, E. Martinez, R. Zivieri, L. Torres, M. Carpentieri, and G. Finocchio, Sci. Rep. **4**, 6784 (2014).

[15] H. Wilhelm, M. Baenitz, M. Schmidt, U. K. Rößler, A. A. Leonov, and A. N. Bogdanov, Phys. Rev. Lett. **107**, 127203 (2011).

[16] S. Seki, X. Z. Yu, S. Ishiwata, and Y. Tokura, Science **336**, 198 (2012).

[17] I. Kézsmárki, S. Bordács, P. Milde, E. Neuber, L. M. Eng, J. S. White, H. M. Rønnow, C. D. Dewhurst, M. Mochizuki, K. Yanai, H. Nakamura, D. Ehlers, V. Tsurkan, and A. Loidl, Nat. Mater. **14**, 1116 (2015).

[18] S. Bordács, A. Butykai, B. G. Szigeti, J. S. White, R. Cubitt, A. O. Leonov, S. Widmann, D. Ehlers, H.-A. K. Nidda, V. Tsurkan, A. Loidl, and I. Kézsmárki, Sci. Rep. **7**, 7584 (2017).

[19] J. S. White, Á. Butykai, R. Cubitt, D. Honecker, C. D. Dewhurst, L. F. Kiss, V. Tsurkan, and S. Bordács, Phys. Rev. B **97**, 020401(R) (2018).

[20] K. Geirhos, B. Gross, B. G. Szigeti, A. Mehlin, S. Philipp, J. S. White, R. Cubitt, S. Widmann, S. Ghara, P. Lunkenheimer, V. Tsurkan, E. Neuber, D. Ivaneyko, P. Milde, L. M. Eng, A. O. Leonov, S. Bordács, M. Poggio, and I. Kézsmárki, npj Quantum Mater. **5**, 1 (2020).

[21] A. Butykai, S. Bordács, I. Kézsmárki, V. Tsurkan, A. Loidl, J. Döring, E. Neuber, P. Milde, S. C. Kehr, and L. M. Eng, Sci. Rep. **7**, 1 (2017).

[22] E. M. Clements, R. Das, G. Pokharel, M. H. Phan, A. D. Christianson, D. Mandrus, J. C. Prestigiacomo, M. S. Osofsky, and H. Srikanth, Phys. Rev. B **101**, 094425 (2020).

[23] A. Butykai, D. Szaller, L. F. Kiss, L. Balogh, M. Garst, L. DeBeer-Schmitt, T. Waki, Y. Tabata, H. Nakamura, I. Kézsmárki, and S. Bordács, arXiv:1910.11523.

[24] V. Ta Phuoc, C. Vaju, B. Corraze, R. Sopracase, A. Perucchi, C. Marini, P. Postorino, M. Chligui, S. Lupi, E. Janod, and L. Cario, Phys. Rev. Lett. **110**, 037401 (2013).

[25] M. M. Abd-Elmeguid, B. Ni, D. I. Khomskii, R. Pocha, D. Johrendt, X. Wang, and K. Syassen, Phys. Rev. Lett. **93**, 126403 (2004).

[26] E. Dorolti, L. Cario, B. Corraze, E. Janod, C. Vaju, H.-J. Koo, E. Kan, and M.-H. Whangbo, J. Am. Chem. Soc. **132**, 5704 (2010).

[27] H.-S. Kim, J. Im, M. J. Han, and H. Jin, Nat. Commun. **5**, 3988 (2014).

[28] V. Guiot, L. Cario, E. Janod, B. Corraze, V. T. Phuoc, M. Rozenberg, P. Stoliar, T. Cren, and D. Roditchev, Nat. Commun. **4**, 1722 (2013).

[29] K. Singh, C. Simon, E. Cannuccia, M.-B. Lepetit, B. Corraze, E. Janod, and L. Cario, Phys. Rev. Lett. **113**, 137602 (2014).

[30] R. Pocha, D. Johrendt, and R. Pöttgen, Chem. Mater. **12**, 2882 (2000).

[31] E. Ruff, S. Widmann, P. Lunkenheimer, V. Tsurkan, S. Bordács, I. Kézsmárki, and A. Loidl, Sci. Adv. **1**, e1500916 (2015).

[32] Z. Wang, E. Ruff, M. Schmidt, V. Tsurkan, I. Kézsmárki, P. Lunkenheimer, and A. Loidl, Phys. Rev. Lett. **115**, 207601 (2015).

[33] D. Ehlers, I. Stasinopoulos, V. Tsurkan, H.-A. Krug von Nidda, T. Fehér, A. Leonov, I. Kézsmárki, D. Grundler, and A. Loidl, Phys. Rev. B **94**, 014406 (2016).

[34] A. O. Leonov and I. Kézsmárki, Phys. Rev. B **96**, 214413 (2017).

[35] A. Mehlin, F. Xue, D. Liang, H. F. Du, M. J. Stolt, S. Jin, M. L. Tian, and M. Poggio, Nano Lett. **15**, 4839 (2015).

[36] B. Gross, D. P. Weber, D. Rüffer, A. Buchter, F. Heimbach, A. Fontcuberta i Morral, D. Grundler, and M. Poggio, Phys. Rev. B **93**, 064409 (2016).

[37] A. Mehlin, B. Gross, M. Wyss, T. Schefer, G. Tütüncüoglu, F. Heimbach, A. Fontcuberta i Morral, D. Grundler, and M. Poggio, Phys. Rev. B **97**, 134422 (2018).

[38] K. A. Modic, M. D. Bachmann, B. J. Ramshaw, F. Arnold, K. R. Shirer, A. Estry, J. B. Betts, N. J. Ghimire, E. D. Bauer, M. Schmidt, M. Baenitz, E. Svanidze, R. D. McDonald, A. Shekhter, and P. J. W. Moll, Nat. Commun. **9**, 3975 (2018).

[39] D. Rugar, H. J. Mamin, and P. Guethner, Appl. Phys. Lett. **55**, 2588 (1989).

[40] E. Neuber, P. Milde, A. Butykai, S. Bordács, H. Nakamura, T. Waki, Y. Tabata, K. Geirhos, P. Lunkenheimer, I. Kézsmárki, P. Ondrejkovic, J. Hlinka, and L. M. Eng, J. Phys. Condens. Mater. **30**, 445402 (2018).